Robust Hadley Circulation changes and increasing global dryness due to CO_2 warming from CMIP-5 model projections

William K. M. Lau[1] and K. M. Kim[2]

[1]Earth System Science Interdisciplinary Center (ESSIC), U. of Maryland

College Park, 20740

[2]Climate and Radiation Laboratory, NASA/Goddard Space Flight Center

Greenbelt, MD 20771

Revised, January, 2015

Submitted to Proceedings of the National Academy of Sciences of the USA

Classification: Physical Sciences (Earth, Atmospheric, and Planetary Sciences)

Title: Robust Hadley Circulation changes and increasing global dryness due to CO_2 warming from CMIP-5 model projections

Authors: William K. M. Lau and K. M. Kim

Affiliation: Earth System Science Interdisciplinary Center (ESSIC), U. of Maryland, College Park, 20740

Corresponding Author: William K-M Lau (wkmlau@umd.edu)

Key Words: Hadley Circulation, CMIP5, Global Warming, Global Dryness, CO_2 Forcing

Abstract

In this paper, we investigate changes in the Hadley Circulation (HC) and their connections to increased global dryness under CO_2 warming from CMIP5 model projections. We find a strengthening of the ascending branch of the HC manifested in a "deep-tropics squeeze" (DTS), *i.e.*, a deepening and narrowing of the convective zone, increased high clouds, and a rise of the level of maximum meridional mass outflow in the upper troposphere (200-100 hPa) of the deep tropics. The DTS induces atmospheric moisture divergence, reduces tropospheric relative humidity in the tropics and subtropics, in conjunction with a widening of the subsiding branches of the HC, resulting in increased frequency of dry events in preferred geographic locations worldwide. Among water cycle parameters examined, global dryness has the highest signal-to-noise ratio. Our results provide scientific bases for inferring that the observed trend of prolonged droughts in recent decades is likely attributable to greenhouse warming.

Significance Statement

In spite of increasing research efforts, global warming signals of the Hadley Circulation (HC) and its dynamical linkages to water cycle changes remain largely unknown. Here, we find from model projections, robust signals of both strengthening and weakening components of the HC induced by CO_2 warming. These changes in the HC drive a pattern of global dryness featuring widespread reduction of tropospheric humidity, and increased risks of drought over subtropics and tropical land. We also find that global warming signal in increased dryness is the most detectable among numerous water cycle quantities examined. Our results provide scientific bases for inferring that the observed trend of prolonged droughts in recent decades is likely attributable to greenhouse warming.

\body

Introduction

The Hadley Circulation (HC), the zonally averaged meridional overturning motion connecting the tropics and mid-latitude, is a key component of the global atmospheric general circulation. How the HC has been, or will be changed as a result of global warming has tremendous societal implications on changes in weather and climate patterns, especially the occurrences of severe floods and droughts around the world (1, 2). Recent studies have suggested that the global balance requirement for water vapor and precipitation weakens the tropical circulation in a warmer climate (3, 4). So far the most robust signal of weakening of tropical circulation from models appears to coming from the Walker circulation, but not from the HC, possibly because of the large internal variability in the latter (5, 6). Observations based on reanalysis data have shown weak signals of increasing, decreasing or no change in HC strength in recent decades, with large uncertainties depending on the data source and the period of analyses (7-10). Meanwhile, studies have also shown that even though water vapor is increased almost everywhere as global temperature rises, increased dryness is found in observations, and in model projections especially in many land regions around the world (11-13). Reduction in mid-tropospheric relative humidity and clouds in the subtropics and midlatitude under global warming have also been noted in models and observations suggesting the importance of cloud feedback and circulation changes (14-16). Even though robust global warming signals have been found in changing rainfall characteristics (2, 17, 18), in the widening of the subtropics, and in the relative contributions of circulation and surface warming to tropical rainfall from climate model projections and observations (19-24), identifying and understanding the dynamical linkages between HC circulation changes and global patterns of wetting and drying have yet to be demonstrated. In this paper, we aim at establishing a baseline understanding of the dynamics of changes in the HC, and relationships with increased global dryness under global warming using monthly outputs from CMIP-5 (Coupled Model Inter-comparison Project) projections. The baseline developed here hopefully will provide guidance for future observational studies in the detection, and attribution of climate change signals in atmospheric circulation and in the assessment of risk of global droughts.

Methodology

To establish the baseline response of the HC to global warming, we used monthly outputs from a 140-year integration of 33 CMIP5 models forced by 1% increase per year CO_2 emission (*SI Method and Data*). The control, also referred to as climatology, is defined as the first 27 years of the model simulation. By the mid-point of the integration, *i.e*., 27-years centered at year-70 of the integration, the CO_2 level is nearly doubled, and by the last 27-year, the mean CO_2 level is nearly tripled (TCO2) compared to the control mean. In this work, we only focused on the forced response, as represented by the Multi Model Mean (MMM) of monthly data, defined as the average of all 33 models interpolated on a common grid resolution of 2.5 by 2.5 degree latitude-longitude, and 17 vertical levels. Anomalies are defined as the MMM differences between TCO2 and the control. The uncertainties of the MMM are estimated from the spread of the individual model means about the MMM, based on calculation of the mean square errors.

Results

Consistent with previous studies (3, 4, 17, 24), we find that in response to a 1% per year CO_2 increase, rainfall increases at a muted rate of 1.5 ± 0.1% K^{-1}[1], much slower than that for saturated water vapor as governed by the Clausius-Clapeyron relationship (~ 6.5% K^{-1}). In the following, the responses of various quantities related to the HC, rainfall, and tropical convection, global dryness and their inter-relationships are discussed.

Rainfall and vertical motions

First, we examine the relationship between zonally averaged rainfall and vertical motions (Fig. 1). Both the climatological MMM rainfall and 500 hPa pressure velocity (Fig. 1a, b) show double maxima in the tropics, consistent with the observed off-equatorial positions of the ITCZ (Inter-Tropical Convergence Zones) (25). Both show the well-known double-ITCZ model bias, *i.e.*, excessive rainfall and too strong rising motions in the southern hemisphere deep tropics (26). The MMM anomalous rainfall shows pronounced increase between 10°S and 10°N, a slight drying in the subtropics, and increased rainfall in the extratropics of both hemispheres (Fig. 1a). The anomalous pressure velocity profile (Fig.1b) shows wavelike perturbations that generally vary inversely with the climatology, featuring enhanced rising motion coinciding with increased rainfall in the deep tropics. Strong compensating anomalous sinking motions are found centered near 10°S and 10°N. Subsiding motions in the subtropics appears to be weakened. Comparing Fig. 1c and d, a structural change in the vertical motion field can be perceived as a shift of the ITCZs of both hemispheres toward the equator, in the form of a narrowing and strengthening of anomalous ascent throughout the troposphere in the equatorial region, flanked on both sides by equally strong descent centered near 10°S and 10°N. The climatological equatorial minimum appears to be filled in by a "squeeze" of the ascending branch of the HC toward the equator from both hemispheres. This "deep–tropics squeeze" (DTS) appears to be coupled to positive anomalies, *i.e.*, weakened sinking motions, near the center of the climatological subsiding branches of the HC. A widening of the subtropics is achieved via the DTS together with a poleward extension (marked by zero-wind contours) of the sinking branch of the HC, and poleward shift of the Ferrel and polar cells in both hemispheres (21, 22). These changes in the HC and related global signals are robust in the sense that more than two-third (25/33) of the models agree on the sign of the anomalies (grid points highlighted by a green dot in Fig. 1d) almost everywhere. Time-series of zonally averaged mean vertical motion clearly show steadily increasing rising motion in the ascending branch of the HC in the deep tropics, throughout the entire 140-years integration (For details, see Fig. S1 and discussions).

Tropical Convection

To better understand the nature of the DTS, we examine the changes in tropical convection and the large-scale tropical circulation. Here, as a proxy for tropical convection, monthly outgoing longwave radiation (OLR) is used. Based on a comparison of observations between monthly OLR from NOAA AVHRR, and daily brightness temperature from TRMM (For details see Fig. S2 and discussions in Supporting Information), and findings from previous studies (27-29), we identify a high monthly OLR ($>270 Wm^{-2}$) with low clouds; a moderate OLR ($270 - 220\ Wm^{-2}$) with middle clouds, and a low OLR ($<220 Wm^{-2}$) with high clouds associated with deep convection. We have computed the MMM climatological probability distribution functions (pdf) of OLR and their changes due to global warming. The climatological OLR pdf (Fig. 2a, b) indicates a weak bimodal distribution of convection in the deep tropics, with an abundance of low to middle clouds, as well as high clouds associated with deep convection (OLR < 220 Wm^{-2}). Near the equator (Fig. 2a), the anomalous OLR profile indicates a shift toward deeper convection, as evident in the pronounced increase in the frequency of lower OLR (colder cloud top) and decrease in higher OLR (warmer cloud top) by 5-15%. At 10^oS-10^oN (Fig.2b), similar shift toward deeper convection can be seen, though the signal is weaker (< 10%) compared to near the equator, due to suppression of deep convection by the anomalous subsidence near 10^oS and N (See Fig. 1). In conjunction with deepening clouds, the anomalous ascent near the equator (Fig. 2c) is enhanced at all levels, most pronounced (up to ~30-40% increase) at upper levels, signaling an upward shift of maximum ascent from the lower to mid- troposphere (700-400 hPa) to the upper troposphere (300-150 hPa). Averaged over 10^oS -10^oN (Fig. 2d), the enhanced ascent in the upper troposphere remains strong (~ 30%), but the anomalous vertical motion below 300 hPa is slightly negative due to strong anomalous sinking motions found near 10^oS and 10^oN, associated with the DTS.

Meridional outflow and relative humidity

The DTS is closely linked to changes in meridional winds of the HC (Fig. 3a). Here, the most prominent feature is a vertical dipole wind anomaly in the tropics, with opposite signs in each hemisphere, *i.e.*, a quadruple pattern, with enhanced outflow away from the equator in the 200-100 hPa layer, and increased inflow between 400-200hPa, toward the equator. Comparing to the control, this indicates a rise in the maximum outflow region in the upper branch of the HC from its climatological maximum level near 200 hPa to 150 hPa. Note that at 200hPa, the anomaly is near zero. A conventional measure of the strength of the HC based on mass outflow at 200hPa (9) would have yielded no significant change in the HC. An examination of the anomalous meridional wind profiles for each model (Fig. S3) indicates that the rise of the maximum outflow region of the HC under global warming is very robust, with all 33 models showing the characteristic quadruple pattern, albeit with varying magnitudes. Time-height cross-sections of the MMM meridional wind profile at 10^o S and 10^o N (Fig. S4) shows clearly a steady rise of the region of maximum outflow as the atmospheric CO_2 loading increases. The meridional outflow mass flux at the upper troposphere (200-100hPa) out of the 10^oS-10^oN zone is estimated to be intensifying at a rate of $+9.8\pm0.7$ [2]% K^{-1}, consistent with an enhancement of the upward motions in the ascending branch of the HC. The effect of the rise in the region of maximum outflow is also evident in the meridional mass streamfunction and zonal winds profile (Fig. S5), reflecting a rise of the center of mass of the entire HC, a poleward expansion of the subtropical subsidence zone (Fig S5a), in conjunction with an upward shift of the westerly zonal wind maxima in the subtropics and midlatitudes (Fig. S5b). The rise in the region of maximum outflow of the HC is also consistent with the increase in tropopause height in the tropics under global warming reported in past studies (30-31). Note that even though the strongest meridional divergent wind is in the upper troposphere, the strongest moisture convergence is confined to the lower and mid-troposphere (Fig. S6), where most of the atmospheric moisture is concentrated.

The roles of atmospheric moist processes and surface evaporation in contributing to the changes in precipitation anomalies are evaluated from the following moisture budget analysis:

$$\langle \overline{P} \rangle = \langle \overline{E} \rangle + \mathrm{ADV} + \mathrm{CONV} + \mathrm{TRS} \qquad \text{Eq (1)}$$

where < > denote vertical average, the ($\overline{}$) denotes monthly mean, and ( )' deviation from the mean; $\overline{P}$ and $\overline{E}$ are monthly mean precipitation and surface evaporation, and ADV = $-\langle \overline{\boldsymbol{V}} \cdot \nabla \overline{q} \rangle$, CONV = $-\langle \overline{q} \nabla \cdot \overline{\boldsymbol{V}} \rangle$, and TRS = $-\langle \overline{\boldsymbol{V}' \cdot \nabla q'} \rangle - \langle \overline{q' \nabla \cdot \boldsymbol{V}'} \rangle$ represents respectively the contribution from moisture advection, dynamic convergence, and transients on shorter time scales. Here, the transients are computed as the residual from Eq (1). Each term in Eq (1) has been computed for the control and for the anomaly. In the control (Fig.3b), clearly surface evaporation in the tropics and subtropics contributes to a large portion of the moisture available for precipitation. However the structure of the precipitation profile in the tropics and subtropics are dominated by CONV, and to a smaller extent by ADV. The effect of TRS appears to be largely in transporting available precipitable water from the subtropics to higher latitudes. Under global warming (Fig 3c), anomalous evaporation contributes ~10-15% of the increased precipitation in the deep tropics, but remains relative constant in latitude, except falling off sharply in the southern hemisphere extratropics. Precipitation anomaly in the deep tropics associated with DTS is dominated by CONV. Between 10^o-30^o latitudes, both CONV and ADV contribute substantially to the precipitation deficit. The contribution from TRS is relatively small in the tropics, but large outside the tropics (>30^o latitudes), and dominant at higher latitudes (>50^o latitudes). In the northern hemisphere extratropics, precipitation anomalies are contributed almost equally by evaporation and TRS, with decreasing contributions from ADV and CONV at higher latitudes. In the southern hemisphere extratropics, TRS contributes to large fraction (> 50%) of the precipitation changes. The TRS has been identified with increased eddy heat and momentum fluxes associated a poleward shift of the storm tracks (21, 32-33[3]). A more detailed discussion of regional contributions by the various processes in Eq. (1) can be found in Supplementary Information (Fig. S7)

The aforementioned changes in HC, and related changes in moisture balance have strong influence on the relative humidity (RH) of the troposphere. The zonally averaged RH anomalous pattern (Fig. 3d) shows a 5-10% reduction, *i.e.*, increased relative dryness, throughout most of the troposphere, except in the lower and mid-troposphere of the deep tropics, and in the lower troposphere of the extratropics and the polar region. This pattern of RH anomaly has been reported in previous studies in the context of cloud radiation feedback and vertical mixing under global warming (15, 34). In this work, we emphasize the physical connection of the RH pattern to changes in the HC. The anomalous RH pattern stems from the different rates of response of moisture convergence and temperature as a function of height and latitude. As a result of CO_2 induced warming, both tropospheric temperature and moisture increase everywhere (Fig. S8). In the deep tropics, below 400hPa, RH is enhanced because of strong CONV (Fig. 3c). However, in the layer from 400-150 hPa, RH is reduced. This is due to faster warming rate in the upper troposphere compare to the lower troposphere, as a result of the moist adiabatic constraint. (See Fig. S6a). Here, high RH air transported from below by CONV, encounters regions of warmer temperature in the upper troposphere, resulting in a deficit of RH. Near 10^o S and 10^o N, the upper troposphere RH deficit is strongly enhanced by increased subsidence associated with negative CONV and ADV (see Fig. 3c), as evident in the two RH minima in the upper troposphere which coincide with the regions of maximum anomalous downward motion at 10^o S and N (See discussion for Fig. 1). In the subtropical mid-to-lower troposphere, the widening of the subsidence zone associated with the DTS brings more dry air from above, increasing the RH deficit. This is reflected in the expanding region of reduced RH from the mid troposphere to the surface in the poleward flank of the climatological dry zones (regions with RH< 40), where the RH deficit is at a maximum. The increased RH near the tropopause and lower stratospheric is associated with the cooling of the lower stratosphere from increased longwave radiative loss to space under global warming (35-36). Even a small increase in moisture due to enhanced vertical transport will result in large increase in RH in these regions.

The association of DTS with the RH changes in the mid and lower troposphere is further examined by regression analysis. The regression map of the 200-150hPa mass outflow at 10^{o}S and 10^{o}N with the 500 hPa RH field (Fig. 4a) shows a quasi-zonally symmetry pattern, indicating positive mass outflow of the HC is associated with increased RH in a narrow swath in the deep tropics along the equator, with the most pronounced signal over the near equatorial regions of the central and eastern Pacific, the Indian Ocean and the Atlantic. Elsewhere globally, RH is mostly reduced, with strong signals found at the poleward flank of the climatology subtropical dry zones (RH<40 in Fig. 4a). The RH deficit is especially pronounced over the southern hemisphere appearing as continuous belt around 30^{o}-60^{o}S. Significant RH reduction is also found over the western Indian Ocean/eastern Maritime continent in connection with increased subsidence associated with a weakened climatological Walker circulation (See also Fig. 4c). At 850hPa (Fig. 4b), the RH regression pattern displays more regional characteristics. Over the longitude sector (160W – 0W), the “squeeze” by the RH deficit zones in the subtropics of both hemispheres toward the strongly increased RH narrow regions of the equatorial central and eastern Pacific and the equatorial Atlantic is very pronounced. The 850 hPa RH deficit pattern corresponds well with regions of large fractional rainfall reduction and enhanced subsidence in the expanded descending branch of the HC (Fig. 4c). Fig. 4c also shows that the DTS is not apparent in the rainfall pattern over the tropical western Pacific and Indian Ocean, where widespread anomalous subsidence dominates, reflecting a weakening of the Walker Circulation under global warming (4-5). The RH 500 hPa and 850 hPa anomaly patterns between TCO2 and control have also been computed, and are found to be very similar to Fig. 4a and b. At the action centers in the polar flank of the subtropical descending zones, the maximum RH deficits are approximately 8-10% [4](See Fig. S9)

DTS and global dryness

To further explore the relationship of HC changes and increased global dryness, we define an extreme dry month at any grid point as a month where the monthly rainfall is less than 0.1 mm/day, and compute the global dryness index (GDI) as the frequency of the occurrence of dry months at every grid point within 60^{o}S-60^{o}N, for all simulated years. The 0-0.1 mm/day range corresponds well with the driest bin in the monthly rainfall pdf of the CMIP-5 models (17). The results shown here are not sensitive to a reasonable range of threshold values used. As shown in Fig. 5a, the climatological GDI pattern matches well with regions of low RH in the climatological 850hPa RH field (Fig. 4b), which can be identified with major regions of deserts, and arid zones around the world. The dominant pattern of anomalous GDI is obtained using Empirical orthogonal function (EOF) decomposition. The principal component of the first EOF which explains a large fraction of the variance (>48%), shows a steady increase in GDI (Fig. 5b) as the CO_2 burden in the atmosphere increases. [5]Region of negative GDI in the tropics appears as a narrow tongue in the equatorial Pacific, coinciding well with regions of RH surplus, and maximum rainfall increase (Fig. 4). Regions of increased GDI are concentrated in preferred geographic locations, *i.e*., the polar flank of the climatological subtropics of Southern Europe and western Asia, South Africa, Australia, and southern Chile; marginal convective zones over the tropical land regions of southwestern North America, central and northern South America and northeastern Brazil. The concentration of pronounced GDI over land regions are likely related to positive feedback from atmosphere-land interactions, arising from large scale dynamical forcing associated with changes in the HC (37-38). The strong east-west asymmetry in the GDI is likely related to changes in rainfall, wind and moist stability in the tropics associated with a weakened Walker Circulation and an altered land-sea thermal contrasts between the western and eastern hemisphere (38). These aspects of research are outside the scope of this paper, and are subjects of ongoing investigations.

As a summary analysis, the temporal changes of aforementioned key circulation parameters related to DTS, and global dryness expressed in percentage change relative to the control as a function of CO_2 loading are shown in Fig. 5c. Relevant statistics of each parameter, including climate sensitivity, R^2 values with DTS outflow are shown in Table 1. All changes appear to be quasi- linear with respect to the CO_2 increase, with high linear regression R^2 value in the range from 0.87-0.99, except for precipitation which has R^2 =0.55. The responses seem to fall into three groups. First is the rapid response group consisting of the 150-200 hPa meridional mass outflow, and the 250 hPa vertical motion in the ascending branch of the HC in 5^o S-5^oN, which increases at a rate of 13.2 % ±1.34 K^{-1}, and 9.9 % ±1.31 K^{-1} respectively with respect to increase in global mean surface temperature. Second is the slower response group with positive trend, including width of the subsidence region (2.3±0.3% K^{-1}), precipitation (3.6 ± 0.3% K^{-1}) and increased high clouds as indicated by frequency of OLR<220Wm^{-2} (2.4±0.26%K^{-1}) in the deep tropics, and the GDI (3.6±0.45%K^{-1}). Third is the slower response group with negative trends, showing decreasing mid-tropospheric RH in the subtropics (-3.1% ±0.17 K^{-1}), and an apparent overall weakening (-2.4% ±0.26 K^{-1}) of the HC according to the conventional measure, *i.e.*, the maximum value of the meridional mass streamfunction in the subtropics (6). The fractional variance of the aforementioned variables explained by DTS mass outflow in the upper troposphere as shown by the R^2 values in Table 1 are uniformly high in the range 0.83 – 0.98, indicating strong coherence with the HC outflow, except for precipitation which has R^2=0.52, indicating much less coherence.

Fig. 5c offers additional information regarding the detectability of global warming signals in HC and water cycle. To estimate detectability, we first construct the 27-year running mean (not show) of all the variables examined so far. The global warming signal is then obtained as the difference of the 27-year running mean with respect to the mean of the first 27 years of the integration, for each quantity we have so far examined. The noise is computed based on the inter-model variability from the MMM. We define the detectability level (DL) as the level of CO_2 in the atmosphere (in percentage) with respect to the control (pre-industrial), at which the signal first becomes statistically significant at the 99% statistical confidence based on a Student's t-test. The DL is meaningful only because of the quasi-linear nature of the responses. Based on the experimental design of 1% per year increase of CO_2, a lower DL represents a more robust signal (higher signal-to-noise ratio) detectable earlier at weaker CO_2 forcing compared to a higher DL. From Fig. 5c and Table 1, in order of increasing DL, the lowest (most detectable) is at 1.18 times of pre-industrial CO_2, for subtropical 500 RH deficit. The next lower DL group in the range of 1.23-1.27

consists of GDI, the upper tropospheric outflow and cloudiness change (OLR) in the deep tropics. This is followed by the next higher DL group at 1.28-1.30 associated with the overall weakening of the HC, enhanced ascent in the rising branch of the HC, and the widening of the subsidence zone. The highest DL (least detectable signal) is found at 1.56 for precipitation in the deep tropics. This is not surprising, since tropical precipitation has the least coherent variability with the DTS signal (lowest R^2 value) and is likely the most difficult to detect due to its inherent noisy nature. Noting that the current climate is at about 1.40 times of pre-industrial CO_2 loading, the DL's estimated here seem to be in broad agreement with numerous published reports of observations of strong signals of mid-tropospheric RH deficit, upper tropospheric moistening, widening of the subtropics and expansion of global dry lands over subtropical land (11-13, 37-40[6]). Nonetheless, it is important to point out that the DL cannot be equated with actual detectability, because of the presence of strong interannual to multi-decadal scale natural variability in the real world. The DL computed here is for MMM, where the natural variability has been minimized. Additionally, estimating detectability from observations has its own practical limitations from lack of long-term reliable data. Hence, actual detectability of global warming signal in the HC and water cycle is likely to be at higher CO_2 level than estimated here. At best, DL can only provide *relative* detectability of the different parameters examined in this paper.

Concluding remarks

In this work, we report new findings regarding robust responses of the HC and their physical linkages to global dryness. Based on analyses of outputs of 33 CMIP5 coupled models, we find both strengthening and weakening signals in the HC responses to a prescribed 1% per year increase in CO_2 emission. The strengthening is associated with a deep-tropics-squeeze (DTS), manifested in the near equatorial regions in the form of a deepening and narrowing of the convective zone, enhanced ascent, increased high clouds, suppressed low clouds, and increased meridional mass outflow ($13.2\% \pm 1.34 K^{-1}$) in the upper troposphere (200-150 hPa), away from the deep tropics. The DTS is coupled to an upward shift of the region of maximum outflow of the HC, a widening of the subtropical subsidence zone, and weakened return inflow of the HC in the lower troposphere. These changes in the large-scale circulation are closely linked to an overall deficit in relative humidity in the upper troposphere of the tropics, and in the middle and lower troposphere of the subtropics, and likely to cloud radiative feedback processes (16, 34). Increasing tropospheric and surface dryness is found at the poleward flank of the climatological dry zones of Africa-Eurasia, and over subtropical land of southwest North America and Mexico and northeastern Brazil. Our results further show that among the various atmospheric water cycle quantities associated with changes in the HC, global warming signal in tropospheric dryness is most likely to be among the first to be detected, manifesting in increased risks of drought in subtropical and tropical land regions.

Acknowledgement

This work is partially supported by Strategic Science Investment fund at the NASA Goddard Space Flight Center, the Precipitation Measuring Mission (PMM), and the Modeling Analysis and Prediction (MAP) program of NASA Headquarters.

References

1. Diaz, H. F., Bradley, R. S. , Eds (2004) *The Hadley Circulation: Present, Past and Future* (Kluwer Academic Publisher), 511p.
2. Dai, A. (2011) Drought under global warming: a review. *WIREs Clim Change* 2: 45–65. doi: 10.1002/wcc.8.
3. Held, I. M., Soden, B. J. (2006) Robust responses of the hydrological cycle to global warming. *J. Climate* 19: 5686–5699.
4. Vecchi, G. A. *et al*., (2006) Weakening of tropical Pacific atmospheric circulation due to anthropogenic forcing, *Nature* 441: 73–76, doi:10.1038/nature04744.
5. Vecchi, G. A., Soden, B. J. (2007) Global warming and the weakening of the tropical circulation. *J. Climate* 20, 4316– 4340.
6. Kang, S. M., Deser, C., Polvani, L. M. (2013) Uncertainty in Climate Change Projections of the Hadley Circulation: The Role of Internal Variability. *J. Climate* 26: 7541–7554. doi: http://dx.doi.org/10.1175/JCLI-D-12-00788.1.
7. Quan, X.-W., Diaz, H. F., Hoerling, M. P. (2004) in *The Hadley Circulation: Past, Present, and Future*, eds Diaz H. F., Bradley R. S. (Springer), pp. 85–120.
8. Mitas, C. M., Clement, A. (2005) Has the Hadley cell been strengthening in recent decades? *Geophys. Res. Lett*. 32, L03809, doi:10.1029/2004GL021765.
9. Tanaka, H. L., Ishizaki, N., Nohara, D. (2005) Intercomparison of the intensities and trends of Hadley, Walker and monsoon circulations in the global warming projections. *SOLA*, 1: 77–80.

10. Waliser, D. E., Shi, Z., Lanzante, J. R., Oort, A. H. (1999) The Hadley circulation: assessing NCEP/NCAR reanalysis and sparse in-situ estimates. *Clim. Dyn*. 15: 719–735, doi:10.1007/s003820050312.
11. Meehl, G., Mu¨nnich, M., Su, H., Meyerson, J. E., Holloway, C. E. (2006) Tropical drying trends in global warming models and observations. *Proc. Natl. Acad. Sci. USA* 103: 6110–6115.
12. Dai A. (2013) Increasing drought under global warming in observations and models. *Nature Climate Change*, 3: 52–58, DOI: 10.1038/NCLIMATE1633
13. Feng, S., Q. Fu (2013) Expansion of global drylands under a warming climate. *Atmos. Chem. Phys*., 13: 10081–10094, www.atmos-chem-phys.net/13/10081/2013/, doi:10.5194/acp-13-10081-2013
14. Fasullo, J. T., K. Trenberth (2012) A less cloudy future: The role of subtropical subsidence in climate sensitivity. Science, 338: 792-793, : DOI: 10.1126/science.1227465
15. Sherwood, S.C. et al. (2010) Relative humidity changes in a warmer climate. *J. Geophys. Res*., 115, D09104, doi:10.1029/2009JD012585
16. Su, H., J. H. Jiang, C. Zhai, T. J. Shen, J. D. Neelin, G. L. Stephens, and Y. L. Yung (2014) Weakening and strengthening structures in the Hadley Circulation change under global warming and implications for cloud response and climate sensitivity, J. Geophys. Res., 119, 5787–5805, doi:10.1002/2014JD021642.
17. Lau, K. M., Wu, H. T., Kim, K.M. (2013) A canonical response in rainfall characteristics to global warming from CMIP5 model projections. *Geophys. Res. Lett*. 40, doi:10.1002/grl.50420.

18. Meehl, G.A., J. M. Arblaster, C. Tebaldi (2005) Understanding future patterns of increased precipitation intensity in climate model simulations. *Geophys. Res. Lett.*, 32, L18719, doi:10.1029/2005GL023680.

19. Frierson, D. M. W., Lu, J., Chen, G. (2007) The width of the Hadley cell in simple and comprehensive general circulation models. *Geophys. Res. Lett*. 34, L18804, doi:10.1029/2007GL031115.

20. Hu, Y., Fu, Q. (2007) Observed poleward expansion of the Hadley circulation since 1979. *Atmos. Chem. Phys*. **7**: 5229–5236.

21. Lu, J., Vecchi, G. A., T. Reichler (2007) Expansion of the Hadley cell under global warming. *Geophys. Res. Lett*. 34, L06805, doi:10.1029/2006GL028443.

22. Seidel, D. J., Fu, Q., Randel, W. J., Reichler, T. J. (2008) Widening of the tropical belt in a changing climate. *Nat. Geosci*. 1: 21–24.

23. Bony, S., G Bellon, D Klock, S. Sherwood, S. Fermepin, S. Denvil (2013) Robust direct effect of carbon dioxide on tropical circulation and regional precipitation. *Nature Geosci.* , doi:10.1038/NGEO1799

24. Richter, I., S.-P. Xie (2008) Muted precipitation increase in global warming simulations: A surface evaporation perspective. J. Geophys. Res., 113, D24118, doi:10.1029/2008JD010561

25. Adler, R. F., Huffman, G. J., Bolvin, D. T., Curtis, S., Nelkin, E. J. (2000) Tropical rainfall distributions determined using TRMM combined with other satellite and rain gauge information. *J. Appl. Meteor.*, 39: 2007–2023.

26. Bellucci, A., Gualdi, S., Navarra, A. (2010) The Double-ITCZ Syndrome in Coupled General Circulation Models: The Role of Large-Scale Vertical Circulation Regimes. *J. Climate*, 23: 1127–1145. doi: http://dx.doi.org/10.1175/2009JCLI3002.1
27. Masunaga, H., Kummerow, C. D. (2006) Observations of tropical precipitating clouds ranging from shallow to deep convective systems. *Geophy. Res. Lett*. 33, L16805, doi: 10.1029/2006GL026547.
28. Lau, K.-M., Wu, H. T. (2011) Climatology and changes in tropical oceanic rainfall characteristics inferred from Tropical Rainfall Measuring Mission (TRMM) data (1998–2009). *J. Geophys. Res*. 116, D17111, doi:10.1029/2011JD015827.
29. Lau K.-M., Wu, H. T. (2003) Warm Rain Processes Over Tropical Oceans and Climate Implications. *Geophys. Res. Lett.* 30, 2290, doi:10.1029/2003GL018567.
30. Wilcox, L. J., Hoskins, B. J., Shine, K. P. (2012) A global blended tropopause based on ERA data. Part II: Trends and tropical broadening. *Q. J. R. Meteorol. Soc*. 138: 576-584. doi:10.1002/qj.910.
31. O'Gorman, P. A., Singh, M. S. (2013) Vertical structure of warming consistent with an upward shift in the middle and upper tropospher. *Geophys. Res. Lett*. 40:1838-1842, doi:10.1002/grl.50328.
32. Woollings, T., J. M. Gregory, J. G. Pinto, M. Reyers, D. J. Brayshaw (2012) Response of the North Atlantic storm track to climate change shaded by ocean-atmosphere coupling. *Nat. Geo*. 5:313-317, doi:10.1038/NGEO1438.
33. Yin, J. H. (2005) A consistent poleward shift of the storm tracks in simulations of 21st century climate. Geophys. Res. Let. 32, L18701, doi:10.1029/2005GL023684.

34. Sherwood, S.C., Bony, S., Dufresne, J-L (2014) Spread in model climate sensitivity traced to atmospheric convective mixing. *Nature*, doi:10.1038/nature12829.

35. Shine, K. P. et al. (2003) A comparison of model-simulated trends in stratospheric temperatures. *Q. J. R. Meteorol. Soc*. 129: 1565–1588.

36. Thompson, D. W. J., et al. (2012) The mystery of recent stratospheric temperature trends. *Nature*, 491: 692- 697.

37. Lintner, B. R., *et al*. (2012) Amplification of wet and dry month occurrence over tropical land regions in response to global warming. *J. Geophys.Res*. 117, D11106, doi:10.1029/2012JD017499.

38. Fu, Q., and Feng, S. (2014) Responses of terrestrial aridity to global warming. *J. Geophys. Res*. 119, doi:101002/2014JD021608.

39. Chung, E.-S., Soden, B., Sohn, B. J., Shi L. (2014) Upper-tropospheric moistening in response to anthropogenic warming. *Proc. Natl. Acad . Sci.* USA, doi:10.1073/pnas.1409659111.

40. Feng, S., and Q. Fu (2013) Expansion of global drylands under a warming climate. *Atmos. Chem. Phys* 13, 10081-10094. Doi:10.5194/acp-13-10081-2013

Figure Legends

Figure 1 Latitudinal profile of MMM (a) rainfall, and (b) 500 hPa vertical motion. Climatology is indicated by red line and anomaly by black line. Open circles indicate where more than 75% (25/33) models agree in the sign of the anomalies. Latitude-height profile of MMM 500 hPa vertical motion for (c) climatology and (d) anomaly. The width of the subsidence zones are indicated by the vertical blue lines. Grid points where more than 25 models agree in the sign of the anomaly are indicated by green dots. Rainfall is in unit of mm day^{-1}, and vertical motion is in unit of negative Pa s^{-1}. Different unit scales are used for climatology and anomalies.

Figure 2 MMM outgoing longwave radiation (OLR) probability distribution function as a function of OLR flux (in Wm^{-2} on y-axis) averaged over (a) 5^oS-5^oN, and (b) 10^oS-10^oN. Vertical profile of mean vertical motion averaged over (c) 5^oS-5^oN, and (d) 10^oS-10^oN. Climatology is indicated by green line and anomaly by blue line. The model spread is shown as yellow shading. The magnitudes of the anomalies have been doubled to enhance clarity. Vertical motion is in unit of negative Pa s^{-1}. OLR pdf is non-dimensional.

Figure 3. Latitude-height cross-section of a) anomalous meridional zonal mean winds (ms^{-1}) and d) anomalous humidity (%). The climatological mean is shown in contour, and anomaly in color. Latitudinal profiles of components of moisture budget for b) the control and c) the anomaly. See text for explanation of symbols. Units in mm day^{-1}.

Figure 4. Spatial pattern of regression of meridional mass flux in the upper troposphere (200-150 hPa) at 10^oS-10^oN with 500hPa RH anomaly (a), and 850 RH anomaly (b).

Climatological dry zones (RH<40 for 500hPa, and RH<50 for 850 hPa) are indicated by orange contours. Also shown are anomaly rainfall pattern (c), with regions of anomalous downward motion stippled. Unit of unit of regression is in percentage change per kg m^{-1}. Unit of rainfall is in percentage.

Figure 5 a) Spatial distribution of eigenfunction of first empirical orthogonal mode of global drought index (GDI), b) principal component of first EOF of GDI, and c) time series of HC circulation and related quantities. See text for detailed definition. Magnitudes are scaled to the mean value in the control (first 27 year of integration), and time is scaled to total CO_2 emission relative to the first year of the integration, with 1% per year increase.

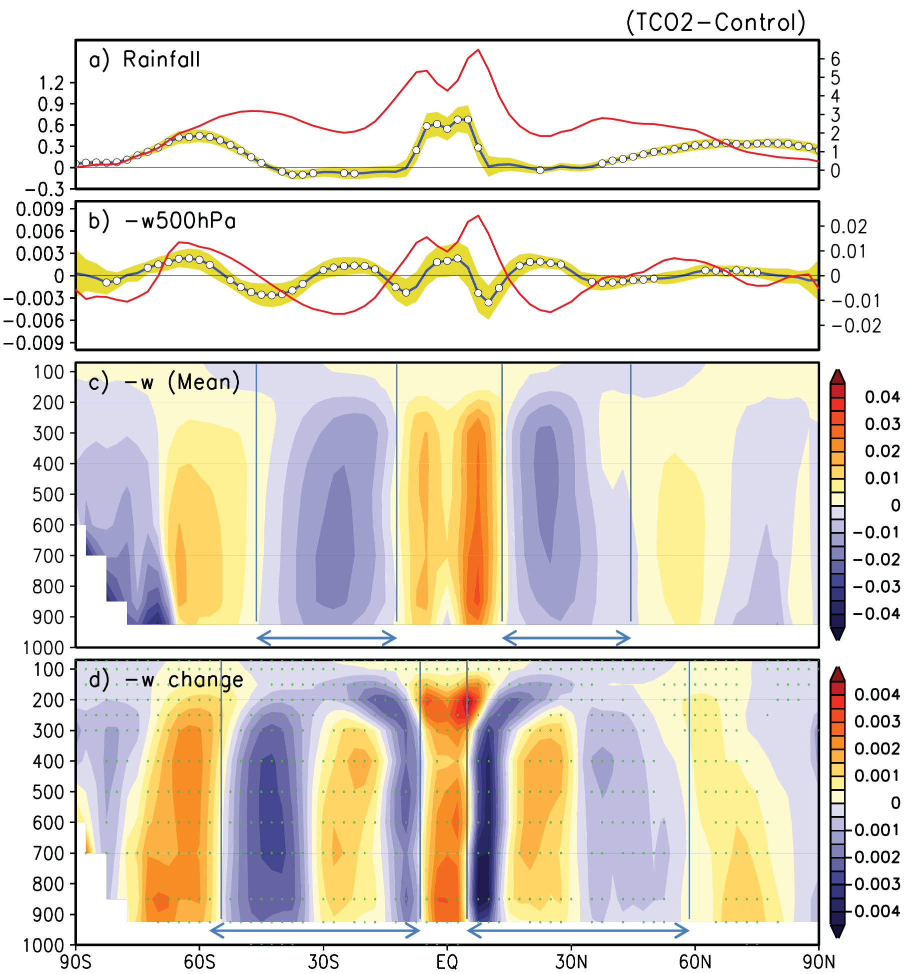
(TCO2−Control)
a) Rainfall
b) −w500hPa
c) −w (Mean)
d) −w change
90S
60S
30S
EQ
30N
60N
90N

Figure 1

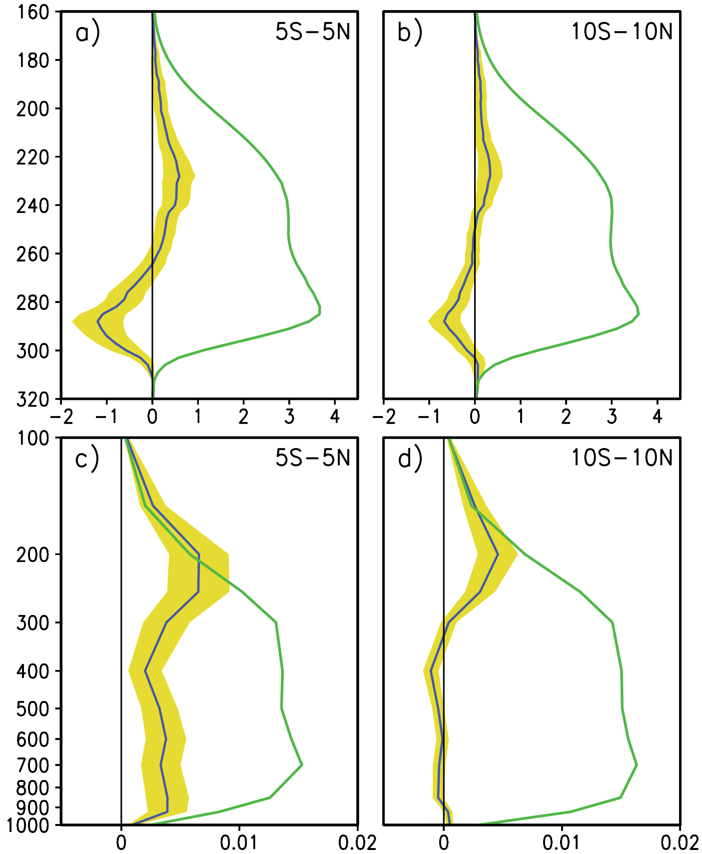

Figure 2

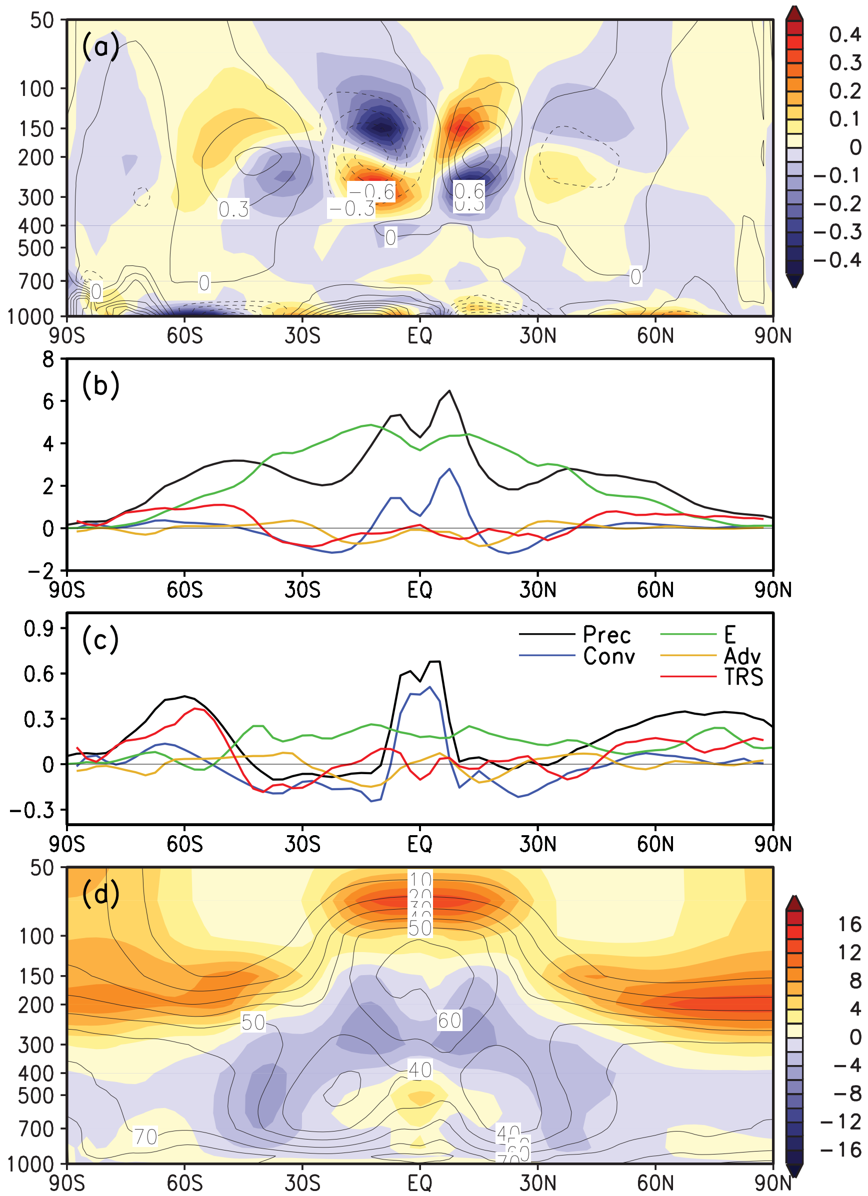
(a)
(b)
(c)
(d)
Prec
Conv
E
Adv
TRS
90S
60S
30S
EQ
30N
60N
90N
50
100
150
200
300
400
500
700
1000
0.4
0.3
0.2
0.1
0
−0.1
−0.2
−0.3
−0.4
−0.6
−0.3
0.6
0.3
8
6
4
2
−2
0.9
0.6
−0.3
16
12
4
−4
−8
−12
−16
10
50
60
40
70

Figure 3

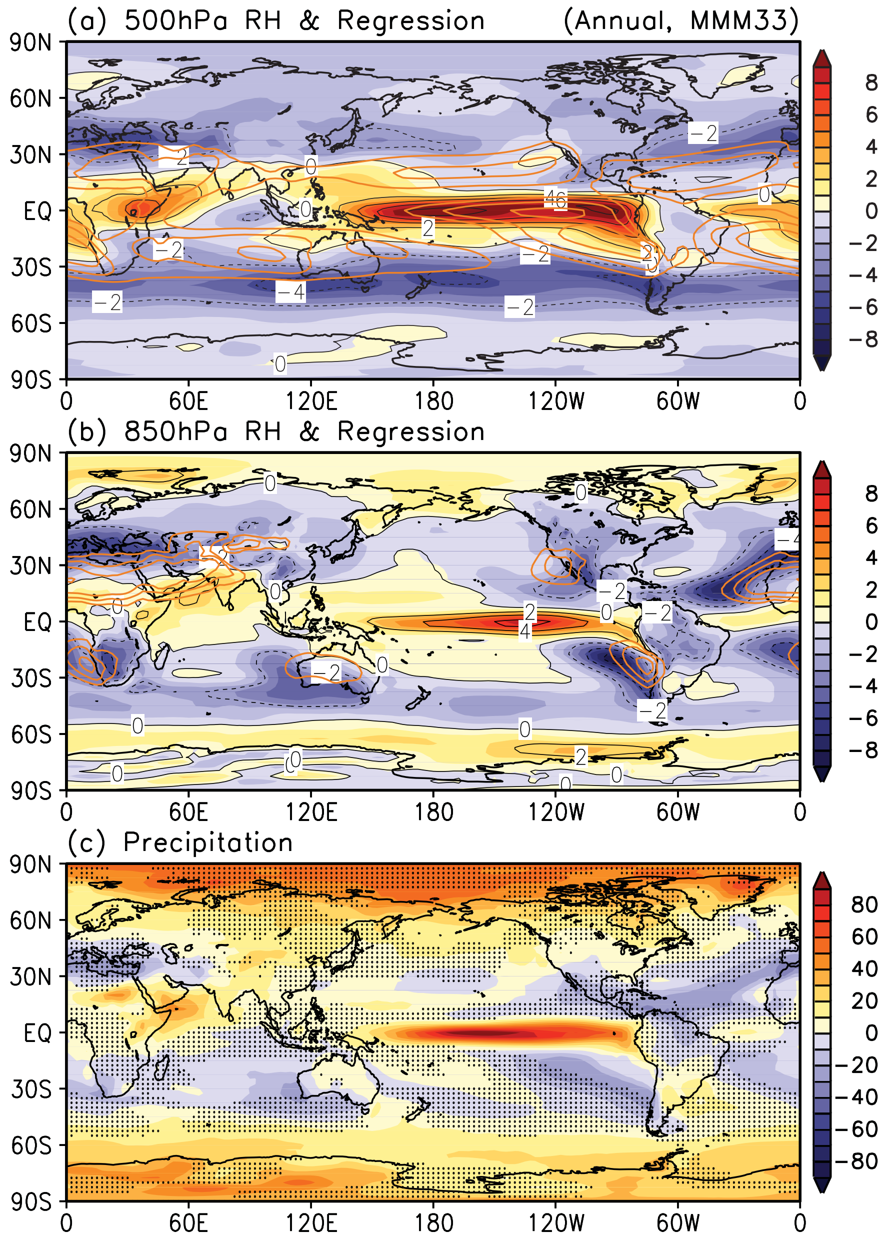
(a) 500hPa RH & Regression
(Annual, MMM33)
(b) 850hPa RH & Regression
(c) Precipitation
90N
60N
30N
EQ
30S
60S
90S
0
60E
120E
180
120W
60W

Figure 4

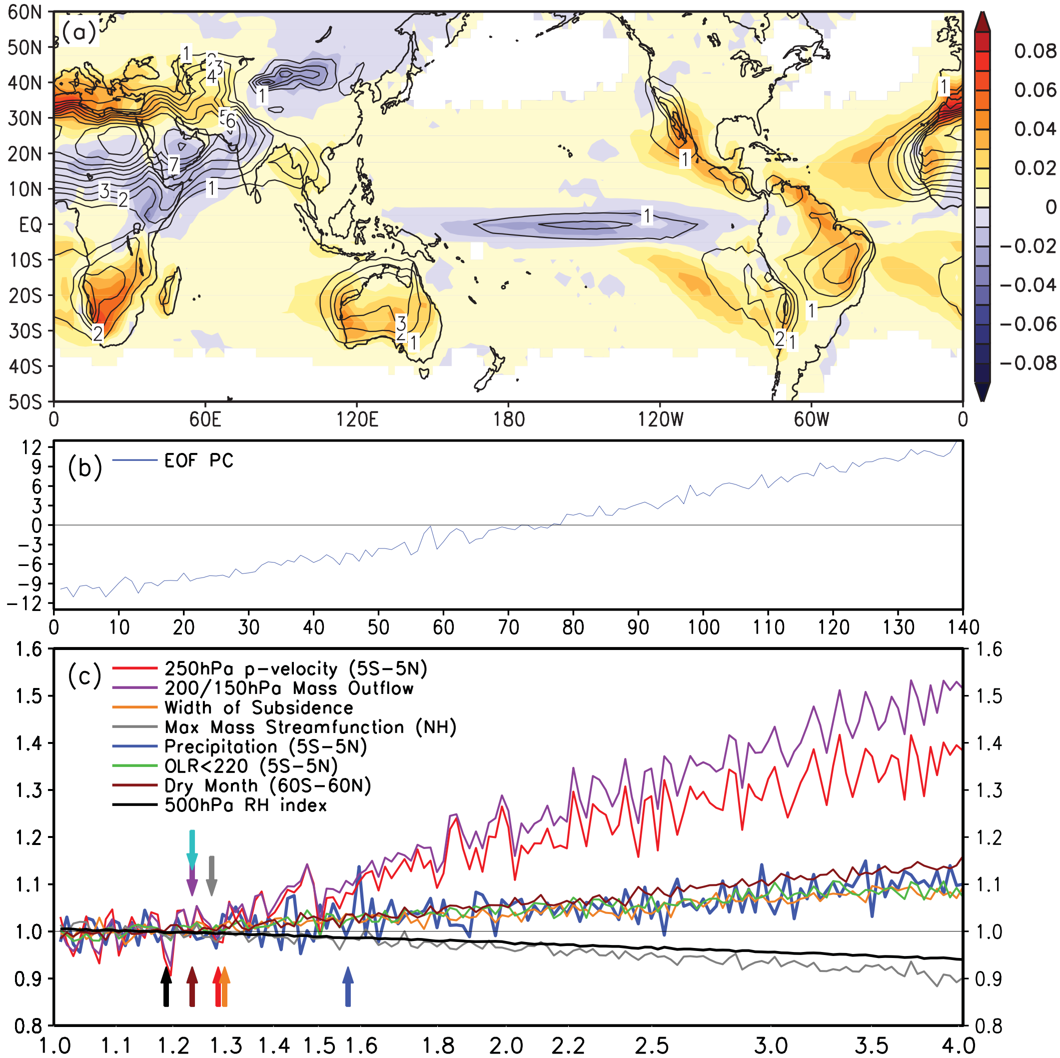
(a)
(b)
EOF PC
(c)
250hPa p−velocity (5S−5N)
200/150hPa Mass Outflow
Width of Subsidence
Max Mass Streamfunction (NH)
Precipitation (5S−5N)
OLR<220 (5S−5N)
Dry Month (60S−60N)
500hPa RH index

Figure 5

Table 1

X	HC outflow	250hPa p-vel	OLR	Precip	Width of Subtropics	GDI	Max. Ψ	500hPa RH
$\frac{\Delta X}{X}$	13.2±1.34	9.9±1.36	2.4±0.82	3.6±0.30	2.3±0.30	3.6±0.45	-2.4±0.26	-3.1±0.17
R2	1.00	0.98	0.91	0.52	0.83	0.92	0.85	0.95
DL	1.23	1.28	1.23	1.56	1.30	1.23	1.27	1.18

Robust responses of the Hadley Circulation and increased global dryness due to CO_2 warming from CMIP5 projections

by

William K. M. Lau and K. M. Kim

Supporting Information

Data and Methods

CMIP5 is the latest model intercomparison project promoted by the World Climate Research Program's Working Group on Coupled Modeling (WCRP WGCM) to provide a framework for coordinated climate change experiments. The scope of CMIP5 include long-term simulations with different of concentration pathways of emission mitigation scenarios, near-term decadal simulations, as well as emission driven Earth System Model (ESM) experiments (1, 2). The 1% per year CO_2 emission increase scenario used for this study applies to a suite of experiments designed to provide a calibration of the model's internal climate variability and response to increasing CO_2 (2). Experiments were started from the pre-industrial levels of CO_2 concentration achieving a quadrupling of CO_2 at the end of 140-year simulation. For this work, we used 33 participating models with various horizontal resolutions, ranging from 0.75 degree to 3.75 degree. Monthly mean winds, vertical motion, and precipitation data are re-gridded to a common grid (2.5^o by 2.5^o). CMIP5 model outputs are available from ESGF (Earth System Grid Federation) gateways (PCMDI, BADC, DKRZ, NCI), and links to ESGF gateways and modeling centers are available from http://cmip-pcmdi.llnl.gov/cmip5/availability.html

S1. Vertical motions

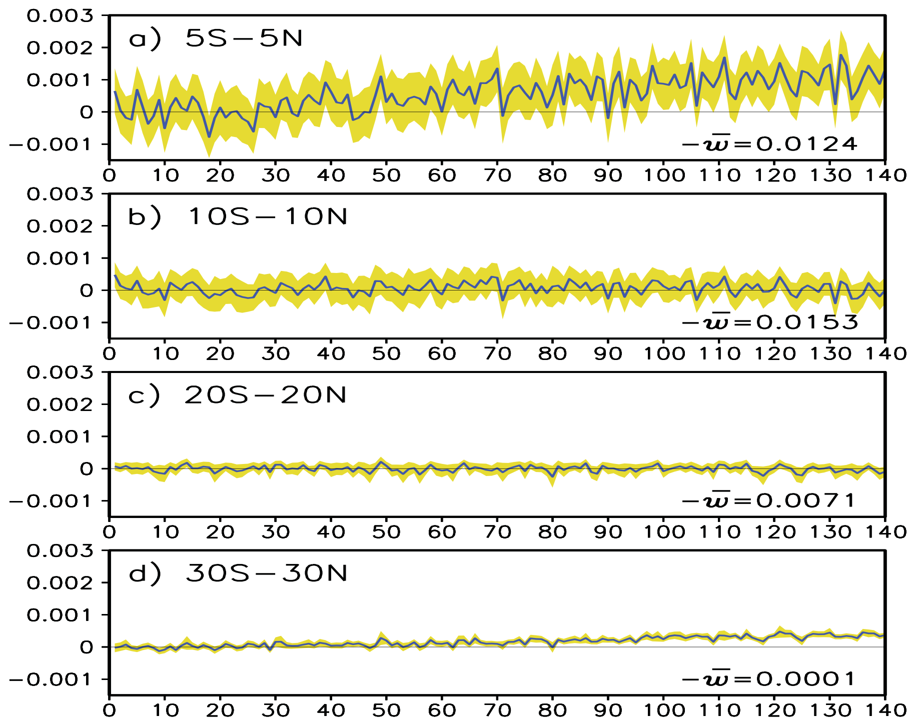

Figure S1 Time series of 140 simulated years of MMM 500 hPa vertical motion averaged between a) 5^oS-5^oN, b)10^oS-10^oN, c) 20^oS-20^oN, d) 30^oS-30^oN, under 1% per year increase CO_2 emission scenario. The MMM is computed from 33 CMIP5 models and the model spread (yellow shading) is the standard errors of the MMM. Unit is negative Pa s^{-1}. The number in the lower right hand corner indicates the MMM vertical velocity in the control.

Changes in the rising branch of the HC, as reflected by the 500hPa pressure velocity averaged over different latitudinal width are shown in Fig. S1. In the near-equatorial regions (5^oS-5^oN), there is a robust increasing trend in upward motion, as indicated by the near constant positive slope (~ 5.2±1.0 % K^{-1}) and the small spread among the models. At wider latitude bands (10^oS-10^oN and 20^oS-20^oN), the changes in vertical motions are substantially muted. When the zonal averages are taken over the entire tropics (30^oS-30^oN), the vertical motions again show a robust rise, but with much smaller amplitude compared to 5^oS-5^oN. Based on the signs of the control and the trends, these results indicate that global warming enhances mean rising motion over the entire tropics (30^oS-30^oN), with the strongest signal coming from the near equatorial region (5^oS-5^oN).

S2. Monthly outgoing longwave radiation (OLR) and daily cloud top temperature

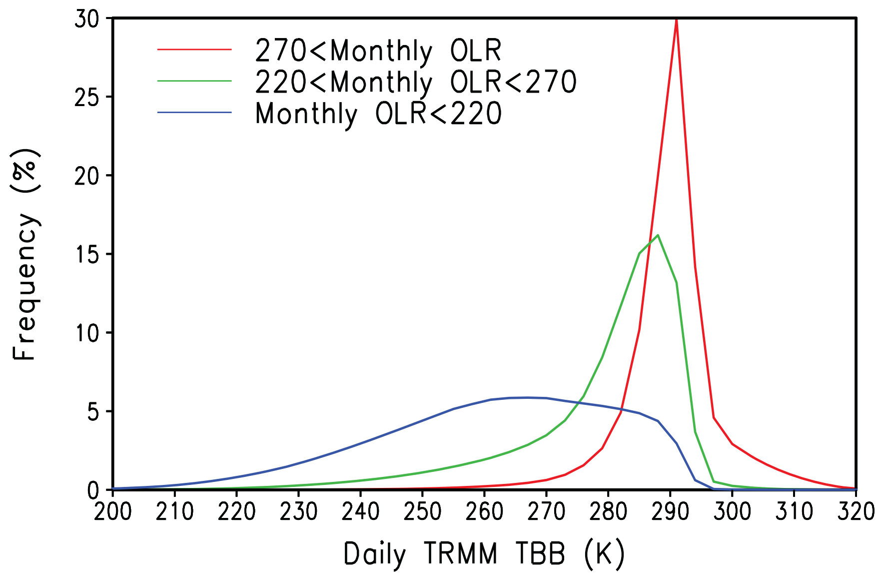

Figure S2 Probability distribution functions of daily T_b for three different monthly OLR bands over the tropics (30S -30N) for the period 1998 – 2012

Monthly outgoing long wave radiation (hereafter OLR) is used as a proxy for tropical convection in this study. To better interpret the physical meaning of OLR with respect to tropical convection, we have investigated the relationship between observed OLR from NOAA AVHRR and daily Visible and Infrared Scanner (VIRS) Channel-4 brightness temperature T_b from TRMM. Figure S2 shows the PDFs of daily T_b corresponding to different bands of OLR. *i.e.*, OLR <220Wm^{-2} (Band 1), 220 Wm^{-2}<OLR<270 Wm^{-2} (Band 2), and OLR> 270 Wm^{-2} (Band 3) used in the main text to describe the physical nature of the cloud system. Here, daily values of T_b = 273K will be identified as the mean freezing level of the standard tropical atmosphere. The PDFs indicate that the three OLR bands are contributed by distinctly different cloud systems as evident in the wide range of T_b distributions with respect to the freezing level. Based on the fraction (α) of the daily population with T_b < 273K, Band 1 (α = 71%), Band 2(α = 25%), and Band 3 (α =3%) can be interpreted respectively as contributions from mostly of ice-phase deep clouds, mixed-phase middle clouds, and warm shallow clouds

S3. Anomalous meridional wind height-latitude cross-sections of individual models

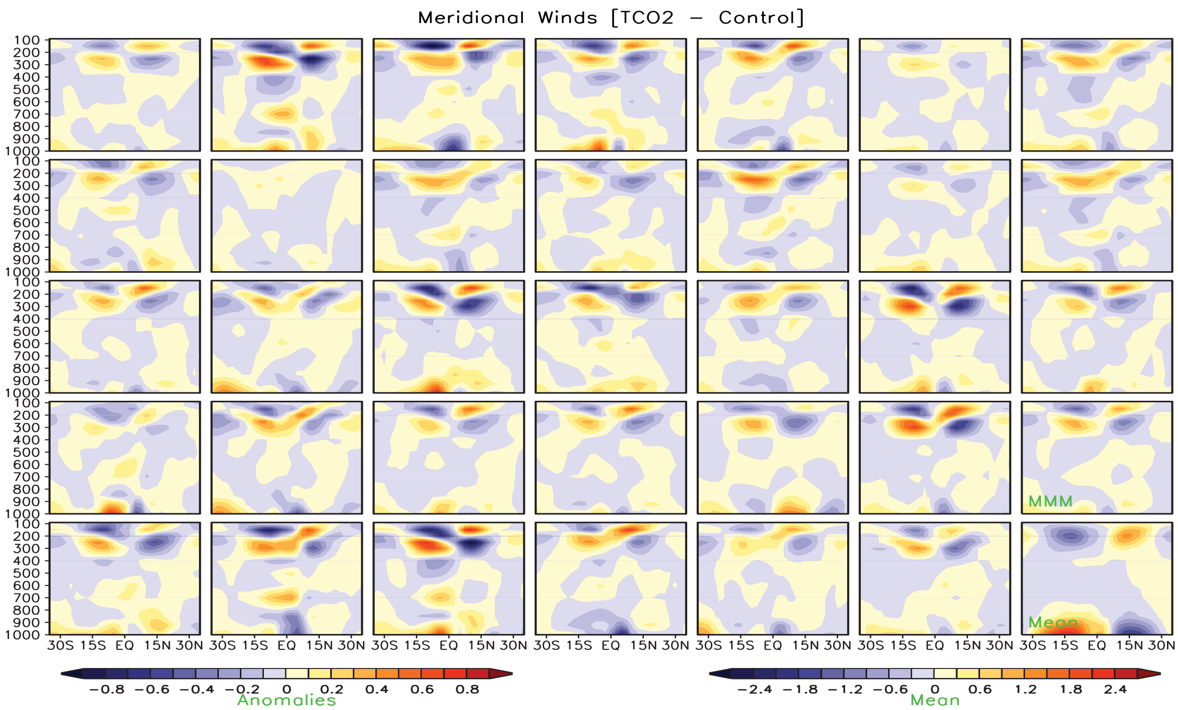

Fig. S3 Latitude-height cross-sections of anomalous meridional winds in the tropics for each of 33 CMIP5 models. The MMM anomaly and control is shown respectively in the bottom two panels of the last column. Unit is in ms^{-1}.

Fig.S3 shows the robustness of the response in the meridional wind as indicated by almost all models showing qualitatively the same response, *i.e.*, a characteristic quadruple pattern in the upper troposphere (<300hPa), signaling a rise of the region of maximum outflow of the HC, and a somewhat weakened return flow in the lower troposphere (>800hPa) and near the surface toward the equator.

S4. Time variation of meridional wind profile

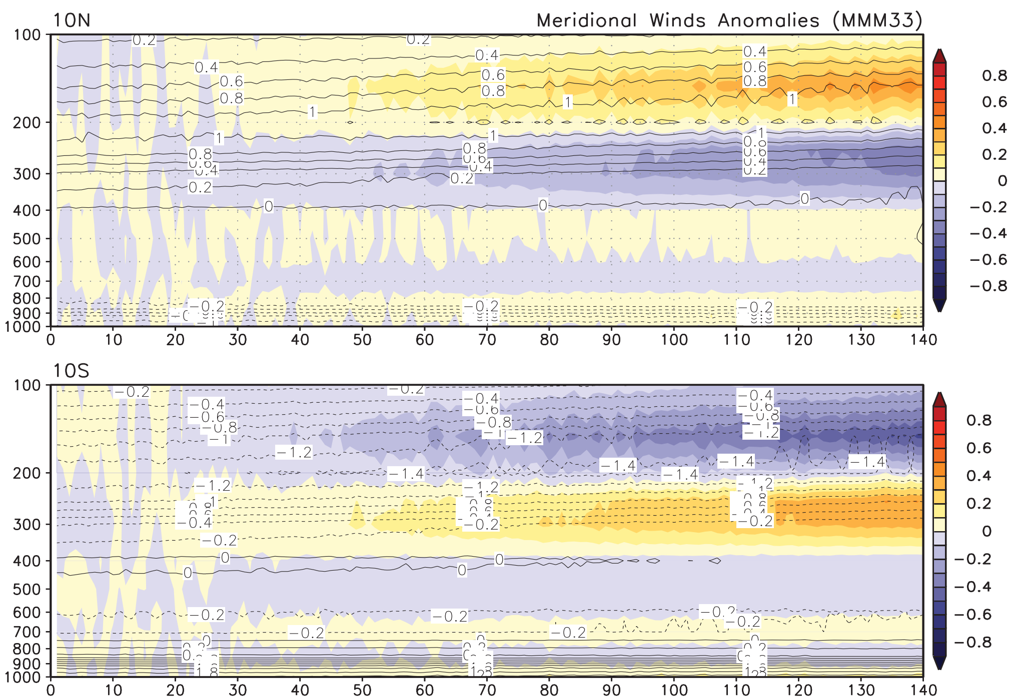

Fig. S4 Time-height cross-section of meridional winds at 10°N (upper panel) and 10°S (lower panel). Units in ms^{-1}.

The time evolution of the meridional wind anomaly at 10° N and S respectively (Fig. S4) shows an increasingly stronger (weaker) outflow above (below) 200 hPa, in both hemispheres, as the CO_2 concentration increases. The near constant positive slopes of the total wind isotachs above 200 hPa reflect a steady rise (~3.5 hPa decade^{-1}) of the region of maximum outflow of the HC. Computations of the meridional mass flux, *i.e.*, mass weighted meridional wind at different cross-sections show that the mass outflow at the upper portion (200-100hPa) out of the 10°S-10°N zone is intensifying at a fast rate of +9.8±0.7 % K^{-1}. The rate of increase is even faster at +17.0±1.7%K^{-1}, out of the 5°S-5°N zone which corresponds to the core ascending branch of the HC. The increased meridional mass flux is compensated by strong inflow in the lower portion

(400-200 hPa) of the climatological outflow region. Even with the strong compensation, the net anomalous mass flux over the climatological outflow region (400-100hPa) out of the 5°S-5°N zone is still increasing, albeit at a much reduced net rate of 1.9±0.8% K^{-1}.

S5. Meridional mass streamfunction and zonal wind

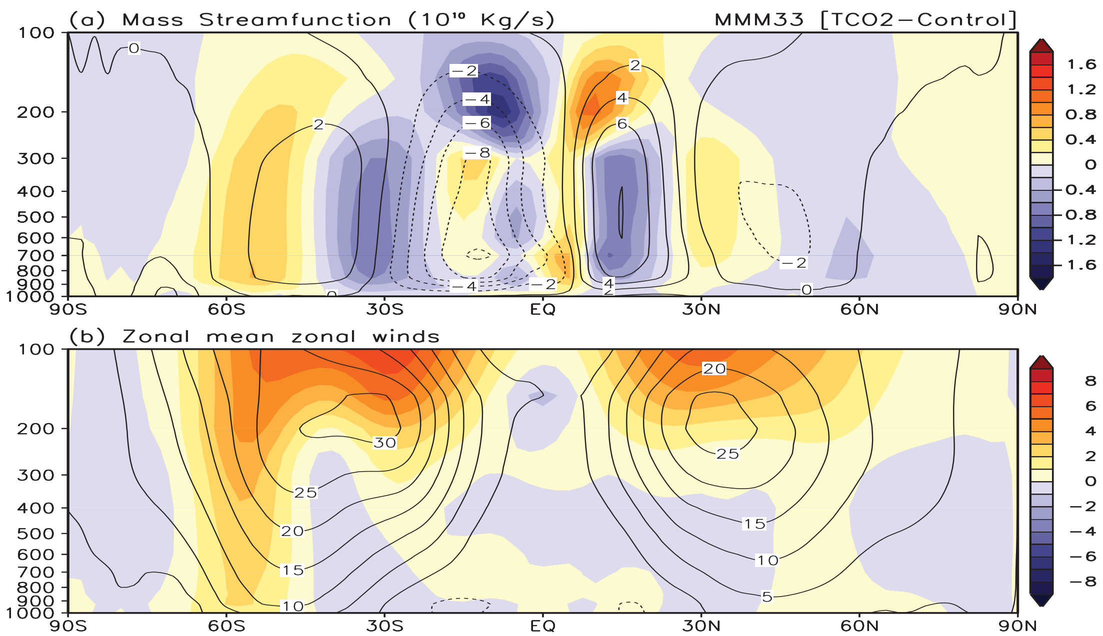

Figure S5 MMM climatology (contour) and anomalies (colored) for a) meridional mass streamfunction, and b) zonal mean winds. Units of mass streamfunction is in 10^{10} Kg s^{-1}, and zonal wind in ms^{-1}.

Changes in the HC associated with the DTS and their connection to the global circulations can also be clearly seen in the anomalous meridional mass streamfunction and zonal winds (Fig. S5). From the signs and locations of the anomalies compared to the control (Fig. S5a), it is clear that the upper branches (above 250 hPa) of the HC in the deep tropics is strengthened, while the lower portion (1000-300 hPa) is weakened, consistent with an elevation of the climatological region of maximum outflow, *i.e.*, a rise of the center of mass of the HC. The rise together with enhanced upper tropospheric vertical motion associated with DTS in the ascending branch of the HC allow stronger poleward outflow in the upper troposphere, thus extending the subsidence branches of the HC in both hemispheres further poleward from their climatological positions. A similar polar extension of the Ferrel cells in both hemispheres, though with much smaller amplitude, can also be discerned. The rise of the center of maximum outflow in the upper branch of the HC is also reflected in changes in the structure of the zonal wind anomaly (Fig. S5b). The most pronounced zonal wind acceleration is found near 100 hPa, above the climatological center at 150- 200 hPa in both hemispheres. The subtropical westerly acceleration in both hemispheres is likely to be driven by the deeper convection, and the Coriolis force from the stronger outflow in the upper troposphere associated with the meridional wind anomalies noted in Fig. 3a in the main text, and Fig.S3. Previous studies have suggested that the extratropical maximum may be related to enhanced baroclinicity due to increased temperature gradient at the upper troposphere, and polar shift of the wintertime storm tracks (4,5).

S6. Latitude-height cross sections of moisture convergence

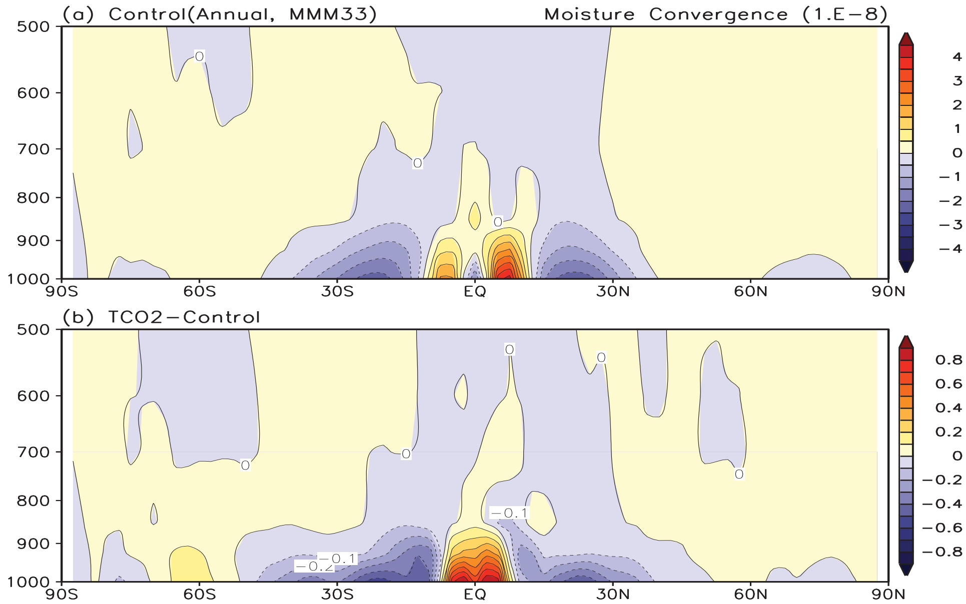

Fig. S6 Latitude-height cross-section of MMM horizontal moisture convergence for a) climatology, and b) anomaly. Unit is in 10^{-8} g $Kg^{-1}s^{-1}$.

The DTS is associated with strong moisture convergence in the lower troposphere in the near equatorial region, and moisture divergence in an expanded subtropical divergence region from 10-50 latitude in both hemisphere (Fig. S6). The moisture convergence increases RH in the lower to mid-troposphere of the deep tropics, and the moisture divergence leads to the RH deficit in the troposphere. As explained in the main text, the RH anomaly pattern is a function of both dynamics and thermodynamics, *i.e.*, more water vapor under warmer condition, and different dynamical feedbacks in the ascending and descending branches of the HC.

S7 Decomposition of precipitation anomalies

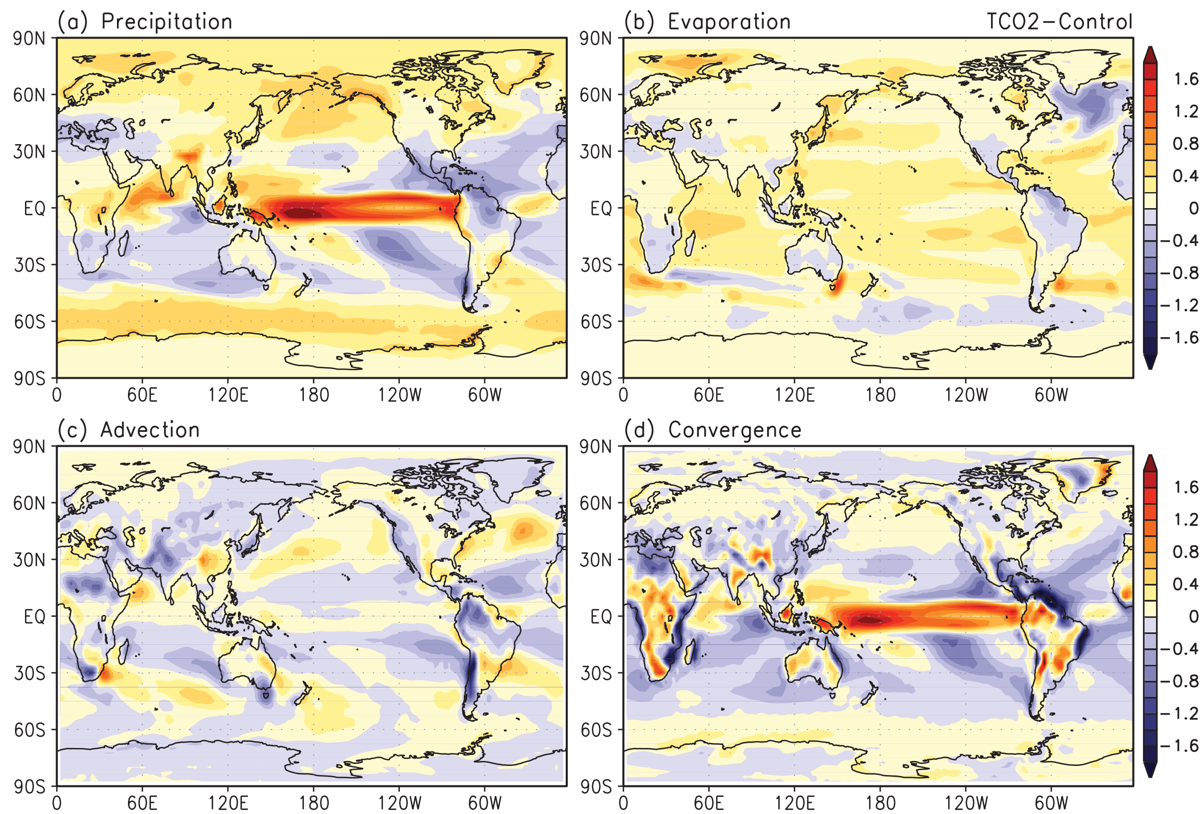

Fig. S7 Anomaly patterns of a) total rainfall, and contributions from b) evaporation, c) advection, d) and dynamic convergence. See main text for explanation. Unit is in mm day^{-1}

The decomposition of total precipitation into evaporation, advection, dynamic convergence, and transients are based on Eq.1 shown in the main text. Comparing the change pattern and magnitude with the total precipitation change (Fig. S7a), it can be seen that evaporation increase, over the ocean almost everywhere, except in the North Atlantic and part of the Southern Oceans, but reduces over land regions in the subtropics, *i.e.*, Southern Europe, northern Africa, South Africa and tropics, *i.e.*, the Maritime continent, southern Australia, Southwest US/Mexico, and Amazonia. However evaporation contribute little to the structure change of the precipitation, *i.e.*, the DTS and drying of the subtropics. Advection (-$\boldsymbol{V} \cdot \nabla q$) contributes strongly to the RH deficit over the west coast of North American, northern South America, Northeast Africa, northern India and northeastern East Asia, and moderately to the drying of the oceanic regions adjacent to the DTS, but not much to the DTS itself (Fig.S7c). The combined effect of negative moisture advection, and reduced evaporation over tropical and subtropical land regions is consistent with the increased GDI over these regions (Fig. 5a), stemming from strong atmosphere-land surface feedback. Clearly from Fig.S7a and d, dynamic convergence ($- q \nabla \cdot \mathbf{V}$) is the major contributor to the structural change of precipitation over the oceanic regions of the tropics and the subtropics, including the DTS, and strong drying in adjacent regions, and broader subtropical regions of the HC. In the equatorial Pacific region, the contribution can be more than 90% of the total precipitation change.

S8. Temperature and moisture response

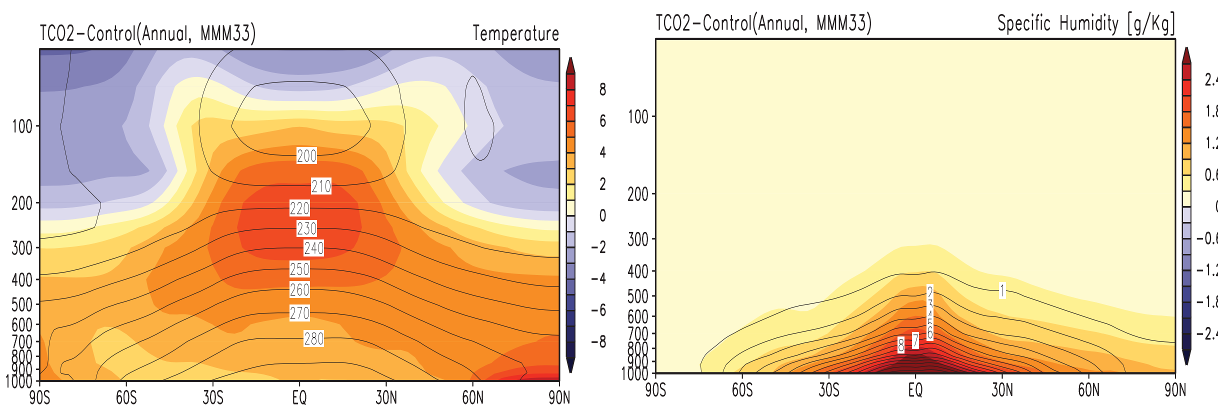

Fig. S8 Latitude-height cross-section of MMM climatology (contour) and anomalies (color) for a) temperature ($^{o}K^{-1}$), and b) specific humidity (g Kg^{-1})

Under a 1% per year increase in CO2 emission, the MMM atmosphere warms by longwave absorption throughout the troposphere up to the tropopause, while the lower stratosphere and regions above cools from reduced longwave radiation from below (Fig. S8). The warming is rather non-uniform. In the tropics, the warming of the upper troposphere is much (> 8^{o}C) stronger than that in lower troposphere (~ 1-2^{o} C) because warm air tends to rise moist adiabatically. At higher latitudes, the warming is mostly confined to the surface and lower troposphere. Tropospheric moisture is increased everywhere following the Clausius Clapeyron law governing saturated water vapor and temperature, with the largest increase in the tropics.

However, because the rapid decrease of moisture with height, the rate of increase of water vapor in the upper troposphere cannot keep up with the accelerated increase in temperature there. As a result, a RH deficit develops in the upper and middle troposphere under global warming. The pattern of RH deficit is further modified by subsidence anomalies associated with changes in the HC as discussed in the main text (Fig 4).

S9 Anomaly patterns relative humidity in the mid- and lower tropospheric

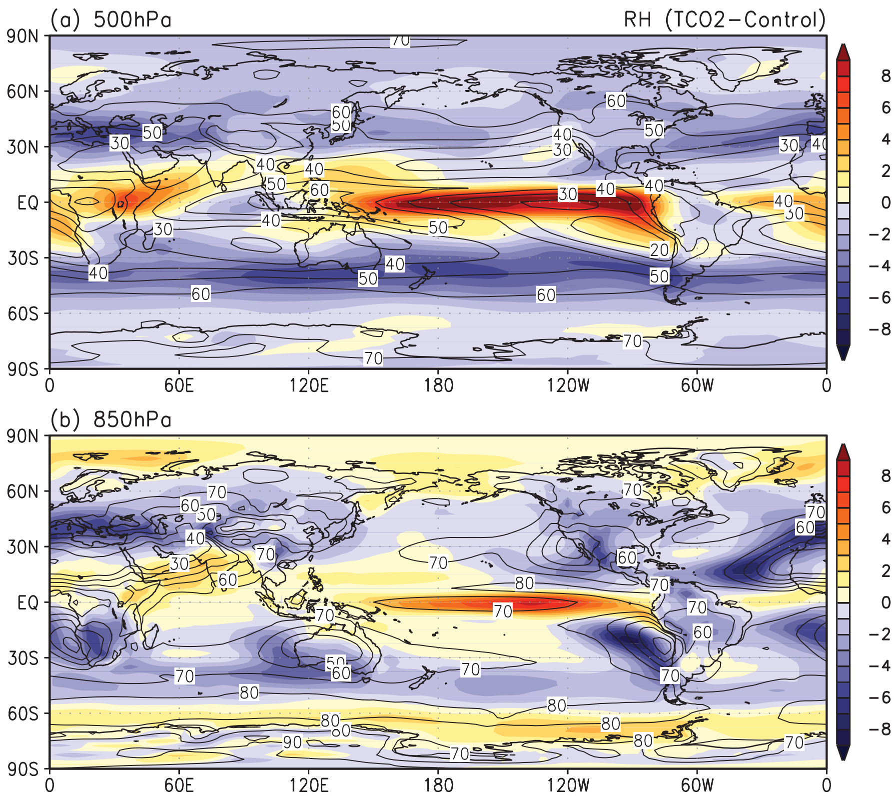

Fig. S9 Anomaly RH patterns at a) 500 hPa and b) 850 hPa, under global warming. Units are in percentage. Climatology is in contour, and anomaly in color

At 500 and at 850 hPa (Fig.S9a and b), the RH pattern is almost identical to the respective regression pattern with DTS upper troposphere outflow (Fig. 4a, and b) in the main text. Key features at 500 hPa includes a) increase RH associated with DTS along the equator, with most prominent signal over the central and eastern equatorial Pacific, b) moderate reduction in RH in the eastern equatorial Indian Ocean and western Maritime continent, Mexico, and Amazonia, and c) prevailing reduction of RH over the rest of the globe, with the strongest signal at the polar flank of the subtropical dry zones. At 850 hPa, the RH pattern shows similar characteristics from a) to c), but with more regionalized features, including strong reduction over land regions of southern Europe and North Africa, South Africa, western Australia, and southern Chile. Other region with large RH deficit include tropical regions of southwestern US, and Mexico, and Amazonia These regions coincide well with regionals of large rainfall deficit, expanded descending branch of the HC (Fig. 4c), and region of maximum GDI (Fig.5a).

References

1. Meehl, G. A., Bony, S. (2011) Introduction to CMIP5. *CLIVAR Exchanges Newsletter*, 16(2): 4-5.
2. Taylor, K. E., Stouffer, R. J., Meehl, G. A. (2012) An overview of CMIP5 and the experiment design. *Bull. Amer. Meteor. Soc*. 93: 485-498, doi:10.1175/BAMS-D-11-00094.1.
3. Liebmann, B., Smith, C. A. (1996) Description of a complete (interpolated) outgoing longwave radiation dataset. *Bull. Amer. Meteor. Soc*. **77**: 1275-1277.
4. Lu, J., Chen, G., Frierson, D. M. W. (2008) Response of the Zonal Mean Atmospheric Circulation to El Niño versus Global Warming. *J. Climate* 21: 5835–5851. doi: http://dx.doi.org/10.1175/2008JCLI2200.1.

5. Kushner, P. J., Held, I. M., Delworth, T. L. (2001) Southern Hemisphere Atmospheric Circulation Response to Global Warming. *J. Climate* 14: 2238–2249.